

Efficient SAR Vessel Detection for FPGA-Based On-Satellite Sensing

Colin Laganier¹, Liam Fletcher¹, Elim Kwan¹, Richard Walters¹, Victoria Nockles¹

Abstract—Rapid analysis of satellite data is vital for many remote sensing applications, from disaster response to environmental monitoring, but is becoming harder to achieve with the increasing volumes of data generated by modern satellites. On-satellite machine learning (ML) offers a potential solution, by reducing latency associated with transmission of these large data volumes to ground stations, but state-of-the-art models are often too large or power-hungry for satellite deployment.

Vessel detection using Synthetic Aperture Radar (SAR) is a critical time-sensitive task for maritime security that exemplifies this challenge. SAR vessel detection has previously been demonstrated only by ML models that either are too large for satellite deployment, have not been developed for sufficiently low-power hardware, or have only been developed and tested on small SAR datasets that do not sufficiently represent the real-world task.

Here we address this issue by developing and deploying a new efficient and highly performant SAR vessel detection model, using a customised YOLOv8 architecture specifically optimized for FPGA-based processing within common satellite power constraints (<10W). We train and evaluate our model on the largest and most diverse open SAR vessel dataset, xView3-SAR, and deploy it on a Kria KV260 MPSoC. We show that our FPGA-based model has detection and classification performance only ~2% and 3% lower than values from state-of-the-art GPU-based models, despite being two to three orders of magnitude smaller in size. This work demonstrates small yet highly performant ML models for time-critical SAR analysis, paving the way for more autonomous, responsive, and scalable Earth observation systems.

I. INTRODUCTION

Rapid analysis of satellite data is vital for a diverse range of remote sensing applications, from environmental surveillance, to wildfire detection, to agricultural monitoring, to disaster response [1]–[4]. However, achieving timely analysis for these applications is increasingly challenging, due to the combination of the difficulty of the analysis itself and the size and continuing growth of satellite datasets. Most analysis tasks for satellite rapid-response applications are computationally hard, requiring accurate extraction, detection or analysis of small-magnitude signals in large, high-dimensional, diverse and noisy datasets (e.g. [5]). And modern satellite constellations generate unprecedented volumes of data over which this analysis must operate, with individual missions often producing terabytes of imagery every day [6]. Machine learning (ML) offers a potential solution by enabling accurate, flexible analysis of large satellite datasets in a fast and automated way (e.g. [7], [8]), but the transfer or downlink of the large raw data volumes to ground-based compute for ML analysis often introduces large degrees of latency to the

processing pipeline, acting as a major bottleneck or rate-limiting-step. On-satellite ML is therefore being increasingly explored as a way to reduce the time from data acquisition to analysis, avoiding the need to downlink full satellite images by running ML algorithms directly on the satellite platform instead (e.g. [9]). However, satellite systems operate with severely restricted power budgets (typically ranging from 2 to 20 watts in CubeSats [10]), limited computational resources, and on a constrained selection of edge processing hardware for which space-hardening is possible (e.g. FPGAs, ASICs). These constraints act to limit the complexity of algorithms that can be deployed onboard satellites, requiring careful design and optimization of ultra-efficient ML processing architectures to achieve required levels of performance and speed of analysis. Therefore, in order to enable near-real-time data analysis for time-critical remote sensing tasks, it is crucial to develop and demonstrate lightweight and highly-performant ML architectures that are suitable for on-satellite deployment. This has only been achieved for a handful of applications to-date (e.g. [11]–[14]), and in this study we tackle this problem for vessel detection with Synthetic Aperture Radar (SAR) satellite data, an important and time-critical application for which on-satellite ML analysis is not yet possible. SAR vessel detection encapsulates and exemplifies the broader motivating issues and barriers to on-satellite ML analysis outlined above, as we now detail in the remainder of this section.

The use of SAR data to detect “dark” ships and other vessels (i.e. those that disable the Automatic Identification Systems (AIS) used for identification and tracking) is critical for maritime surveillance; including for monitoring illegal fishing activities [15], combating maritime piracy [16], and for intercepting trafficking operations [17]. SAR satellites are highly suited for this and other rapid-response tasks due to their all-weather, 24-hour, active imaging capabilities [18]. Many maritime surveillance applications require the ability to detect and classify ships in near-real-time for rapid response (e.g. to intercept illegal activities or coordinate emergency response), ideally within minutes of data acquisition [19].

However, reliable vessel detection from SAR imagery is a demanding task, even for sophisticated algorithms. Vessels have a small pixel footprint (of order 10 pixels long) relative to SAR scenes (30,000 pixels wide, contrast Fig. 1b and c-e), are similar in spatial extent and amplitude to background clutter (e.g. see Fig. 1c-e), and the inherent speckle noise in SAR images and high variability in vessel signatures across different sea states further complicates separation of vessels and background [20]. These challenges are especially

¹The Alan Turing Institute, British Library, 96 Euston Rd., London NW1 2DB, United Kingdom claganier@turing.ac.uk

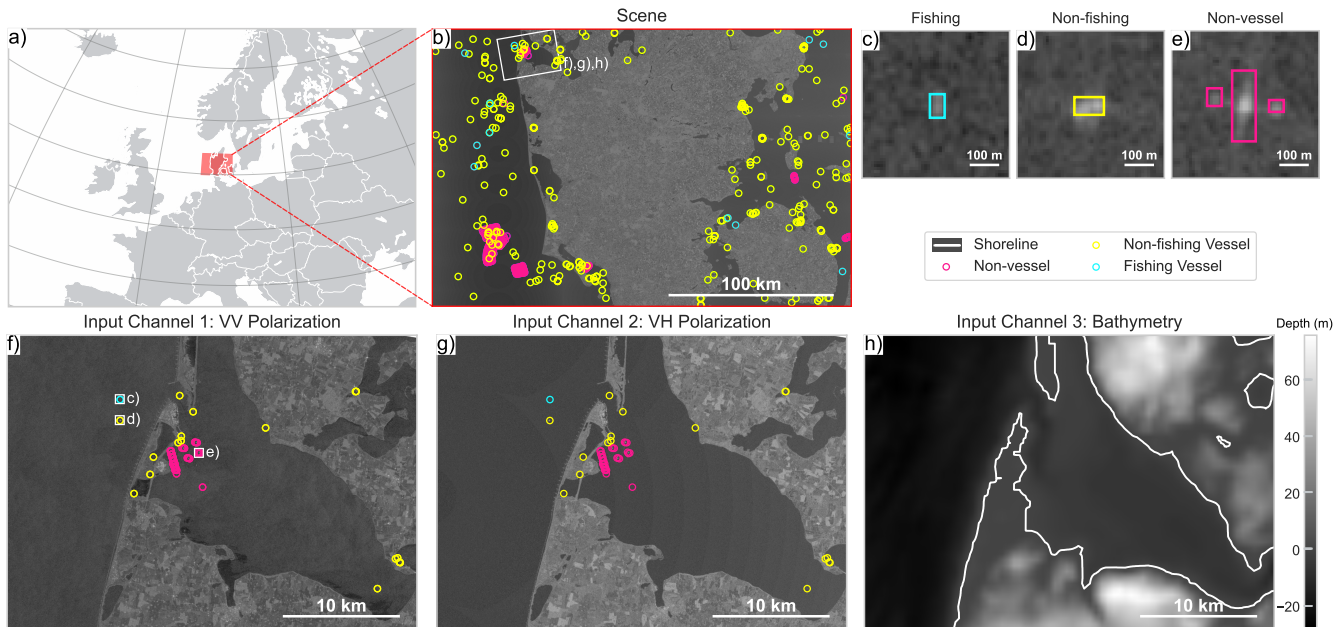


Fig. 1. Example imagery from our dataset to illustrate the SAR Vessel Detection Task. (a,b) Single Sentinel-1 SAR scene over the Netherlands from the xView3-SAR dataset. (b) shows amplitude of the VH band for the full scene with coloured circles denoting ground truth fishing vessel (cyan), non-fishing vessel (yellow) and non-vessel (magenta) objects. (c-e) show sample close-up images of fishing vessel (c), non-fishing vessel (d) and non-vessel objects (e). (f-h) show the three channels used as model input in this study, for the highlighted region in (b); VV band SAR amplitude (f), VH band SAR amplitude (g) and bathymetry (h).

pronounced in near-shore regions, making the task harder in these areas [21]. Together, the combined characteristics of the SAR data and the detection task necessitate advanced processing techniques that can effectively and reliably separate genuine vessel signatures from the complex maritime environment, whilst also maintaining high detection accuracy across diverse operational conditions.

Furthermore, the size of SAR datasets also presents a significant challenge for near-real-time vessel detection systems. Modern SAR satellites such as Sentinel-1, ALOS-4 and NISAR [22]–[24] each generate multiple terabytes of imagery every day, with individual scenes often spanning hundreds of kilometers in width (e.g. see Fig. 1a-b) and containing gigabytes of data at high spatial resolution (tens of meters). Analyzing such large datasets requires substantial computational resources and memory bandwidth, particularly when implementing sophisticated detection algorithms that analyze all pixels in an image to search for potential vessel signatures. In addition, this problem is growing as increasing numbers of SAR satellites, with higher resolution and larger imaging footprints, lead to ever-increasing data throughput [25].

The recent development of computer vision techniques for SAR vessel detection [26] has addressed the challenges associated with task difficulty and dataset size, enabling automated, adaptable and robust analysis of very large datasets, and representing a significant advance in accuracy and adaptability compared to traditional rule-based methods [27], [28]. These deep learning methods leverage large-scale datasets to learn and extract features across diverse

operational conditions, improving their ability to generalise relative to traditional statistical methods. But ML approaches still cannot yet be used for rapid near-real-time analysis. The large volumes of data create storage and transmission bottlenecks, making it impractical to downlink all collected imagery for ground-based ML analysis in rapid-response scenarios. In order to achieve near-real-time analysis, on-satellite edge ML architectures for SAR vessel detection are needed, which would enable satellites to autonomously identify dark vessels and reduce the delay between observation and operational response.

But despite recent advances, efficient, state-of-the-art and deployable SAR vessel detection models do not yet exist. State-of-the-art models achieve high accuracy across diverse maritime conditions (e.g. as represented by the largest and most diverse open SAR vessel dataset; xView3-SAR [29]), but achieve this through use of large-scale architectures and ensemble methods, which means they are too large and power-hungry for satellite deployment (the top 5 performing models from the competition associated with the xView3-SAR dataset have 89M to 754M parameters; 249 MB to 3.0 GB [29]; see blue symbols in Table I and Fig. 3). In contrast, various lightweight models for SAR vessel detection have been proposed, using a range of architectures such as LSR-Det [30], SAR-Net [31], and YOLO [32]–[34]. But the majority of these models have either not been deployed or evaluated on edge hardware [30]–[34], or else have been developed for and tested on platforms with power requirements exceeding satellite constraints [35]. Finally, the only models that have been deployed on hardware with low enough power

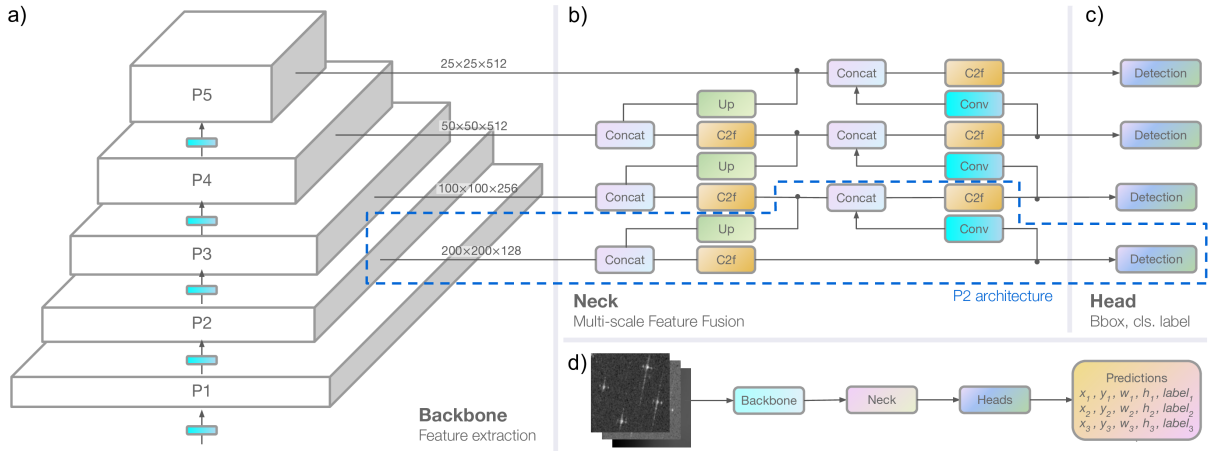


Fig. 2. Architecture diagram of the YOLOv8-based object detection model. (a) feature extraction backbone, (b) multi-scale feature fusion neck, (c) detection head, (d) simplified end-to-end detection pipeline from SAR and bathymetry input to final predictions. P2 architecture branch is shown in dashed blue box. Diagram modified from [42].

to meet these constraints (Field-Programmable Gate Arrays; FPGAs [36]–[38]) have only been trained and evaluated on relatively small and less representative SAR vessel datasets [39]–[41] that do not reflect the real-world scale, diversity, and complexity of operational maritime scenarios captured in large-scale benchmarks such as xView3-SAR (which has 1-2 orders of magnitude more ship instances and 2-3 orders of magnitude more image pixels). In summary, SAR vessel detection has previously been demonstrated only by ML models that either are too large for satellite deployment, have not been developed for sufficiently low-power hardware, or have only been developed and tested on small SAR datasets that do not sufficiently represent the complexity of the real-world task.

In this study, we address this gap by developing an efficient and highly-performant SAR vessel detection methodology, optimized for on-satellite deployment. Our main contributions are:

- We design and deploy a new efficient and highly performant SAR vessel detection model, using a customised YOLOv8 architecture specifically optimized for FPGA-based processing. We train and evaluate our model on the largest and most diverse open SAR vessel dataset, xView3-SAR (in contrast to previous FPGA-based SAR vessel detection models) and deploy it on an AMD/Xilinx Kria KV260 platform using Vitis AI.
- Our model is between ~ 130 and ~ 1500 times smaller than top-performing xView3-SAR competition models, whilst achieving near state-of-the-art performance in detection and classification (distinguishing between vessels, fishing vessels, and maritime infrastructure) on the xView3-SAR dataset.
- The final system operates on an FPGA with a sub-10 watt power budget, and can process a 40,000 km² SAR scene in under one minute, demonstrating its suitability for time-sensitive, resource-constrained satellite missions.

II. METHODOLOGY

In this study we use the YOLOv8 architecture [43] (Fig. 2) as our base model, due to its previous use for both SAR vessel detection [44], [45] and small object detection [46]. In Section II-A we describe the base YOLOv8 detection model architecture, the range of modifications to YOLOv8 that have been previously suggested for SAR and small object detection, and our own proposed model architecture, which combines three of these modifications. We then detail our FPGA deployment in Section II-B, followed by an overview of the xView3-SAR dataset in Section II-C. Finally, we describe our evaluation metrics in Section II-D and the training setup for our models in Section II-E.

A. YOLOv8 and Proposed Model Architecture

YOLOv8 is a recent iteration of the YOLO architecture family [43], introducing anchor-free detection alongside improvements in both accuracy and processing speed relative to previous versions. At its core, the model’s feature extractor is a modified CSPDarkNet53 architecture [47], which incorporates five downsampling operations from $2\times$ to $32\times$ and produces the scaled output feature maps P1-P5. This backbone (Fig. 2a) relies on Cross Stage Partial (CSP) blocks for feature extraction, specifically an optimized CSP block with two Conv modules (*Convolution-BN-SiLU*) and n bottlenecks, referred to as C2f blocks. The SPPF (Spatial Pyramid Pooling - Fast) module further enhances the final stage of the backbone by aggregating multi-scale spatial information. The baseline architecture feeds the P3, P4, and P5 feature maps—of dimensions 100×100 , 50×50 , and 25×25 , respectively, for a 800×800 pixel input—into the model’s neck. This neck (Fig. 2b) employs a Path Aggregation Network (PAN) Feature Pyramid Network (FPN) [48] [49] structure that effectively combines multi-scale feature maps in both a top-down and bottom-up network structure. The YOLOv8 heads (Fig. 2c) separate object classification, using binary cross-entropy loss, from bounding box regression, employing a combination of Distribution Focal Loss (DFL)

and Complete IoU (CIoU) to achieve more precise object localization and classification.

1) *SAR & Small Object Detection*: First we briefly review existing literature on SAR vessel detection and small object detection using the YOLOv8 framework, in order to inform our methodology. Prior work has introduced various architectural and functional modifications to improve small target detection, which can be broadly grouped into two categories: architectural enhancements (including adjustments to convolutional blocks, FPN structures, and attention mechanisms) and alternative loss functions, tailored to small object localization.

Modified convolutional blocks have been employed to enhance detection performance, to reduce computational complexity, or both. [44] implemented GhostConv and RepGhost bottlenecks to reduce model size without compromising representational capacity, whereas [50], [51] replaced C2f blocks with C3 blocks, incorporating GhostConv bottlenecks to enhance the efficiency of small object detection. [45] utilized Partial Convolution (PConv) as an alternative approach for improving feature learning efficiency on SAR scenes.

FPN modifications have also been proposed to improve SAR detection. To preserve fine-grained spatial details essential for small target identification, [52], [53] incorporated the P2 feature map, which captures higher-resolution features lost in deeper layers. [52] further added an Asymptotic Feature Pyramid Network (AFPNet) to improve multi-scale feature fusion, while [46] implemented a Generalized Feature Pyramid Network (GFPN) for small-object detection in non-SAR contexts.

Attention mechanisms have also been widely adopted to improve feature discrimination in cluttered SAR imagery. [44] implemented ShuffleAttention to model channel-wise dependencies, and both [45], [52] employed Efficient Multi-scale Attention (EMA [54]) modules to enhance cross-scale feature representation. [55] demonstrated improved localization of small objects in non-SAR images by applying Coordinate Attention (CA [56]) to embed precise positional information within channel attention.

In addition to architectural innovations, several alternative loss functions have previously been explored to enhance localization accuracy. [44] used Wise IoU (WIoU) loss, which dynamically adjusts focus based on anchor quality through a non-monotonic penalty mechanism. [45] adopted MP-DIoU loss to improve overlap estimation by minimizing distances between the corners of predicted and ground truth boxes. Finally, for non-SAR small-object tasks, [46] implemented the Powerful IoU (PIoU) loss, which reduces localization error by minimizing the Euclidean distance between corresponding corners of bounding boxes.

2) *Proposed Architecture*: Our proposed architecture incorporates three of these modifications to enhance small object detection performance whilst maintaining computational efficiency. In our experiments we also tested a variety of the broader set of modifications detailed in the previous section; for brevity we do not discuss those here, but illustrative results showing why they were not incorporated in our final

architecture are presented in Table I and discussed briefly in Section III-A.

First, to better leverage multi-scale feature representations, we extend the FPN by incorporating the P2 feature map alongside an additional detection head (Fig. 2). While higher-resolution shallow feature maps (P1, P2) provide superior capability for capturing fine-grained details essential for small target detection, deeper features (P4, P5) effectively detect larger objects.

Second, we introduce two architectural improvements to enhance performance while reducing computational overhead. We replace the C2f blocks with CSP blocks featuring three Conv modules (referred to as C3), which incorporate an additional Conv module and enhance feature representation with minimal computational overhead. We also substitute the up- and down-sampling Conv blocks in the backbone and neck, as well as those in the bottleneck modules, with GhostConv [57]. This lightweight convolution variant reduces both computational and parameter overhead by generating feature maps through a two-stage process; a primary convolution produces a low-dimensional representation ($\lfloor c_{out}/2 \rfloor$ channels), which is then concatenated with the output of a secondary depthwise convolution of matching dimensions.

Third, to address the inherent challenges of small object detection, we replace the standard IoU loss with PIoU [58]. This modified loss function incorporates two key mechanisms: an adaptive penalty factor based on target size, calculated from the average absolute distance between corresponding edges of prediction and ground truth boxes, and a non-monotonic focusing mechanism that concentrates learning on bounding boxes with moderate prediction quality, thereby improving convergence on challenging small objects.

B. FPGA Deployment

We evaluate our proposed solution on the AMD/Xilinx Kria KV260 board, which integrates programmable logic (PL; featuring 117,120 LUTs, 234,240 FFs, 1,248 DSP slices, 144 MB BRAM, and 64 MB URAM) with a processing system (PS) based on a Quad-core Arm Cortex-A53 SoC. For model deployment, we utilized the Vitis AI 3.5 framework and created a custom hardware design targeting the PL of the Kria KV260 and incorporating the Deep Learning Processing Unit (DPU) 4.1 IP using Vivado 2023.2. The DPU is a programmable engine optimized for deep neural networks, which is leveraged by the Vitis AI instruction set to run models in the PL. In our design, the DPU is configured with one B4096 core and a clock frequency of 300 MHz. We quantized the model to INT8 using the Vitis AI Quantizer library, using symmetric quantization with a power-of-two scaling scheme, allowing for both Post-Training Quantization (PTQ) and Quantization-Aware Training (QAT) using a straight-through estimator [59]. The DPU of the Kria KV260 platform (DPUCZDX8G) does not support the SiLU activation function used in YOLOv8, and therefore we modified the model to use Hard Swish activations [60] instead. Finally, we deployed the compiled model on the FPGA using the Vitis AI Runtime, and evaluated

model performance in terms of speed, power consumption, and accuracy.

C. Dataset

The xView3-SAR [29] dataset is a large-scale collection of high-resolution SAR maritime images. The dataset contains 754 publicly available images (an additional 237 images are held privately and not publicly accessible), with an average size of 29,400 by 24,400 pixels. The scenes are C-band SAR images acquired by the European Space Agency’s (ESA’s) Sentinel-1 constellation; specifically the Interferometric Wide Swath mode Level-1 Ground Range Detected product, which includes both vertical-horizontal (VH) and vertical-vertical (VV) polarization bands for each image at a 10-meter pixel spacing. The scenes have gone through a pre-processing step, including orbit correction, removal of noise artifacts, radiometric calibration, terrain correction, and geocoding. In addition to the VH and VV SAR images, ancillary data is provided including wind speed, direction, quality, and land/ice mask information from Sentinel-1 Level-2 Ocean product, as well as bathymetry information from the General Bathymetric Chart of the Oceans [61]. These have been co-registered with the respective SAR scenes and are provided in the xView3-SAR dataset at a lower resolution than the SAR images, with 500-meter pixel spacing. The scenes are distributed over four distinct geographical regions in European waters (Adriatic, Bay of Biscay, Iceland, and Norway) and one in West African waters (Gulf of Guinea).

The xView3-SAR competition dataset provides annotations and labels for maritime object detections derived from two sources: the AIS database and manual expert reviewers. AIS is a radio transponder system used for collision avoidance that broadcasts ships’ GNSS coordinates. The labels include detection coordinates (and associated pixel coordinates), detection class, bounding box coordinates and dimensions, length, distance from shore and confidence score. Detection class labels include: non-vessels, which are detections of fixed infrastructure such as wind farms, fish cages, platforms, and port towers; fishing vessels; and non-fishing vessels. An example scene is shown in Fig. 1a,b.

The dataset is divided into training, validation, and test sets containing 554, 50, and 150 scenes, respectively. The training set contains only automatically labeled detections (i.e. AIS only) while the others contain both expert-reviewed AIS detection and manually-labeled detections. Consequently, the training dataset lacks manually annotated bounding boxes and is generally of lower quality, with occasional mismatches between bounding boxes and detected objects caused by the automated matching process. Additionally, some fixed infrastructure is missing ground-truth labels, and because many vessels do not broadcast AIS signals in near-shore areas, the training set contains approximately 100× fewer near-shore detections as a proportion of total detection than the validation set.

D. Evaluation Metrics

To evaluate our models we use the test dataset, which contains 60,010 detections. We evaluate predictions using four metrics from the xView3-SAR competition, to measure the models’ detection and classification performance across the different scenes. The metrics are:

- 1) Detection F1-score, evaluating the model’s capacity to identify maritime objects across different sea states, geographical areas and SAR acquisition configurations.
- 2) Near-shore F1-score, evaluating the model’s detection performance on maritime objects that are within two kilometers from shore (as defined by the zero-point in co-registered bathymetry data), in typically higher vessel density areas.
- 3) Vessel Classification F1-score, evaluating model performance at identifying whether a maritime object is a “vessel” or “fixed infrastructure” (non-vessel). This classification is only performed on manual labels with a high or medium confidence score, or that are identified via correlation with AIS.
- 4) Fishing Classification F1-score, evaluating the model’s performance in identifying fishing and non-fishing vessels. This classification is evaluated with AIS labels.

This evaluation allows for direct comparison and benchmarking of our model to the models from the top-5 winning entries to the xView3-SAR competition [29]. The evaluation metrics for these models are reported in the top section of Table I (blue symbols). The trained model weights and code for these models were also made available by competitors, as well as for the competition reference model (Faster R-CNN ResNet50), and are used for comparison with our own model in Fig. 4. The competition also provides a vessel length estimation metric which is not used in this work, as our focus is on detection and classification performance, and length prediction is less relevant for our application.

E. Training Setup

Our training methodology employs two different datasets and two distinct training strategies to generate our final model. We utilize both the xView3-SAR training *and* validation sets for training; the latter offers higher-quality annotations (see section C above), and has consistently demonstrated superior detection performance when used as a training set, both in our experiments and in prior competition-winning solutions. To structure our experiments, we therefore partitioned the xView3-SAR validation set into 40 scenes for training and 10 scenes for validation. These subsets are referred to as the *training* and *validation* sets throughout this work; the former is used for our initial exploratory analysis and for fine-tuning our final models. Additionally, we addressed the limitations of the automatically-generated labels in the original xView3-SAR training set by generating pseudo-labels and bounding boxes using our best-performing exploratory model (YOLOv8n-Ghost-P2-PIoU2 trained for 100 epochs). This enhanced dataset is referred to hereafter as the *pre-training* set.

For initial model exploration (Table II.A-D), we trained models on the *training* set for 100 epochs using AdamW (batch size: 16, learning rate: 1.429×10^{-3} , momentum: 0.9, linear warm-up: 3 epochs). For final model development (Table II.E), we adopted a two-stage training procedure. In the pre-training stage (**PT**), the model was trained for 100 epochs on the pseudo-labeled *pre-training* dataset using AdamW (batch size: 32, learning rate: 7.14×10^{-4} , momentum: 0.9, linear warm-up: 3 epochs). This was followed by a fine-tuning stage (**FT**), in which the model was trained for another 100 epochs on the *training* set using stochastic gradient descent with momentum (batch size: 16, learning rate: 5×10^{-3} , momentum: 0.9, no warm-up). Finally, we applied an Adaptive Threshold (**AT**) strategy that adjusts the confidence threshold of predictions based on two factors: the predicted class label (non-vessel, non-fishing vessel, fishing vessel) and proximity to shore (defined as within 2 km of the shoreline or not). We used the *validation* set to determine the optimal threshold for each of the six classes by selecting the value that maximized the detection F1-score.

We trained all models using the Ultralytics codebase with PyTorch 2.4.1 and CUDA 12.1 on a NVIDIA A100 GPU (40GB). The model input consisted of three channels; VV and VH SAR bands along with bathymetry data (e.g. see Fig. 1f-h and Fig. 2d), with scenes partitioned into 800 by 800 pixel chips using a tiling approach. SAR channel amplitudes were clipped to the range [-50, 20] dB, while bathymetry values were clipped to [-6000, 2000] meters, with each channel subsequently linearly normalized to the range [0, 255] for model input. We incorporated negative samples (background chips containing no detections) into the training data after identifying that this approach improved overall model detection performance by 1.8%. Consequently, we implemented a 30% background ratio in the model training data, with background chips randomly sampled from the pre-processed dataset. To enhance model generalization, we implemented standard image augmentations, including mosaic augmentation, random translations, scaling, left-right flips, image blurring, and hue-saturation-value adjustments.

III. RESULTS

We present the results of training the different YOLOv8 architectures in Section III-A, followed by the evaluation of the quantized model in Section III-B, and finally report the performance of the deployed model running on FPGA hardware in Section III-C.

A. Model Modification Results

The model size, computational complexity and performance on the test dataset for a representative range of the various model architectures we have explored through our analysis are presented in Table I.

Our analysis of different YOLOv8 model sizes (n , s , m and l) demonstrates that smaller architectures consistently outperform larger ones across most metrics (Table I.A). The smallest model (*nano*) achieves superior performance compared to the largest variant, with improvements of 2.4% in

overall detection and 7.4% in near-shore detection. Similarly, in classification the *nano* model’s accuracy is within 0.3% of larger models for vessel classification, with minor variation across model size observed, while it outperforms the larger models by up to 1.4% in fishing classification. This inverse relationship between model complexity and performance aligns with the observations in [62] and suggests that the maritime detection task may benefit from simpler, more generalizable feature representations that avoid overfitting to training data complexities and errors in AIS locations. We also note that this relationship could alternatively be caused by larger models requiring more training data to achieve optimal performance, but we do not pursue this further here because our focus in this paper is on lightweight models, for which the smaller YOLOv8 variants are more suited.

Building upon the *nano* baseline architecture, we explored efficiency-enhancing modifications that could maintain performance while reducing computational requirements. The integration of Ghost convolutions into the bottleneck layers proves particularly effective (Table I.B), delivering a 45% reduction in model size and FLOPs while improving fishing classification performance by 1.5% at the cost of a 0.3% drop in overall detection. We also evaluated alternative efficient convolutional blocks from the literature, such as EfficientNet, ShuffleNet, and FasterNet [63]–[65]. These architectures achieved less substantial reductions in model size (ranging from 1.8-2.6M parameters compared to Ghost’s 1.7M) while delivering comparable or slightly inferior performance, indicating that Ghost convolutions provide a more effective balance of efficiency and detection performance for this task.

The performance gains from architectural efficiency are further enhanced through multi-scale feature representation. Incorporating higher-resolution P2 feature maps into the *nano* Ghost architecture yields substantial benefits (Table I.C), particularly for challenging near-shore detection scenarios where vessels must be distinguished from coastal infrastructure, with near-shore detection performance increasing by 7.6% compared to the baseline YOLOv8n-Ghost. While adding the P2 features increases computational complexity by 27.5%, the Ghost convolution’s gains in efficiency offset this increase, keeping the final FLOPs equivalent to the baseline YOLOv8n model. Ablation studies confirm the importance of multi-scale features, as removing the P5 feature map (YOLOv8n-Ghost-P2-3-4) results in performance degradation of 0.7% and 0.4% in overall detection and fishing classification respectively compared to the P2 architecture.

Building on these architectural improvements, we examined loss function variants specifically designed for small object detection. Among the evaluated alternatives to the baseline CIoU loss, PIoU2 demonstrates superior performance (Table I.D), providing consistent improvements of 1.4% in overall detection and 0.7% in fishing classification. In contrast, using MPDIoU loss results in improvements of 0.3% and 1.3% in classification but a decline in overall detection performance, while WIoU shows consistent performance drops across all metrics compared to CIoU.

From these architecture evaluation experiments, the

TABLE I

PERFORMANCE OF YOLOV8 DETECTION MODELS ON THE xVIEW3-SAR DATASET. SUBHEADINGS INDICATE THE SPECIFIC MODEL ARCHITECTURE AND TRAINING VARIATIONS EXPLORED. ARCHITECTURES HIGHLIGHTED IN BOLD REPRESENT THE SELECTED CONFIGURATIONS CARRIED FORWARD TO THE FINAL MODEL (★). xVIEW3-SAR COMPETITION MODELS ARE LISTED AT THE TOP, WITH THE NUMBER OF MODELS IN ENSEMBLES IN PARENTHESES. COLORED SYMBOLS CORRESPOND TO MODELS ILLUSTRATED IN FIG. 4. F1-SCORES FOR SUBSECTIONS A-E ARE PROVIDED AS MEANS AND STANDARD DEVIATIONS OVER THREE RANDOM SEEDS.

Model	Params (M)	Size (MB)	FLOPs (G)	F1-Score			
				Detection	Near-Shore	Vessel	Fishing
xView3-SAR Competition Models [29]							
● CircleNet (12)	322.5	1294	-	0.755	0.525	0.942	0.834
■ UNet (6)	432.5	1732	-	0.752	0.473	0.938	0.803
◆ HRNet (15)	754.3	3029	-	0.730	0.467	0.932	0.828
▼ Faster R-CNN	89.1	249	-	0.726	0.428	0.954	0.822
▲ HRNet (12)	328.1	1314	-	0.725	0.461	0.940	0.797
A) Model Size							
YOLOv8l	43.7	175.4	165.2	0.607 \pm 0.006	0.293 \pm 0.020	0.895 \pm 0.014	0.684 \pm 0.021
YOLOv8m	25.9	104.1	78.9	0.627 \pm 0.014	0.364 \pm 0.009	0.913 \pm 0.004	0.679 \pm 0.008
YOLOv8s	11.2	45.1	28.6	0.622 \pm 0.007	0.362 \pm 0.006	0.915 \pm 0.001	0.684 \pm 0.010
YOLOv8n	3.2	12.6	8.7	0.631 \pm 0.008	0.367 \pm 0.017	0.912 \pm 0.006	0.693 \pm 0.009
B) Convolutional Block							
YOLOv8n-EfficientNet	2.6	11.4	7.3	0.630 \pm 0.003	0.367 \pm 0.013	0.911 \pm 0.003	0.708 \pm 0.006
YOLOv8n-ShuffleNet	1.8	7.6	5.3	0.626 \pm 0.002	0.352 \pm 0.002	0.904 \pm 0.004	0.685 \pm 0.002
YOLOv8n-FasterNet	1.9	8.4	5.8	0.628 \pm 0.005	0.359 \pm 0.003	0.912 \pm 0.003	0.704 \pm 0.007
YOLOv8n-Ghost	1.7	7.6	5.1	0.628 \pm 0.002	0.361 \pm 0.007	0.912 \pm 0.001	0.708 \pm 0.011
C) P2 Feature Map							
YOLOv8n-Ghost-P2-3-4	1.1	4.6	8.3	0.664 \pm 0.003	0.435 \pm 0.005	0.919 \pm 0.003	0.701 \pm 0.003
YOLOv8n-Ghost-P2	1.6	7.8	8.8	0.671 \pm 0.002	0.437 \pm 0.004	0.918 \pm 0.003	0.705 \pm 0.006
D) Bounding Box Loss							
YOLOv8n-Ghost-P2-MPDIoU	1.6	7.8	8.8	0.664 \pm 0.002	0.437 \pm 0.002	0.921 \pm 0.006	0.718 \pm 0.010
YOLOv8n-Ghost-P2-WIoU	1.6	7.8	8.8	0.670 \pm 0.004	0.420 \pm 0.025	0.908 \pm 0.014	0.697 \pm 0.022
YOLOv8n-Ghost-P2-PIoU2	1.6	7.8	8.8	0.685 \pm 0.001	0.436 \pm 0.004	0.917 \pm 0.004	0.712 \pm 0.008
E) Two-Stage Training							
YOLOv8n (PT)	3.2	12.6	8.7	0.621 \pm 0.001	0.289 \pm 0.004	0.873 \pm 0.003	0.693 \pm 0.008
YOLOv8n (FT)	3.2	12.6	8.7	0.632 \pm 0.007	0.379 \pm 0.011	0.928 \pm 0.002	0.741 \pm 0.013
YOLOv8n (FT+AT)	3.2	12.6	8.7	0.650 \pm 0.002	0.385 \pm 0.008	0.918 \pm 0.003	0.737 \pm 0.016
YOLOv8s-Ghost-P2-PIoU (PT)	5.3	22.6	22.3	0.692 \pm 0.002	0.328 \pm 0.007	0.869 \pm 0.001	0.756 \pm 0.002
YOLOv8s-Ghost-P2-PIoU (FT)	5.3	22.6	22.3	0.694 \pm 0.003	0.448 \pm 0.014	0.932 \pm 0.002	0.769 \pm 0.011
● YOLOv8s-Ghost-P2-PIoU (FT+AT)	5.3	22.6	22.3	0.703 \pm 0.004	0.444 \pm 0.010	0.928 \pm 0.003	0.770 \pm 0.013
YOLOv8n-Ghost-P2-PIoU (PT)	1.6	7.8	8.8	0.686 \pm 0.001	0.324 \pm 0.002	0.865 \pm 0.003	0.743 \pm 0.003
YOLOv8n-Ghost-P2-PIoU (FT)	1.6	7.8	8.8	0.691 \pm 0.003	0.450 \pm 0.003	0.929 \pm 0.003	0.767 \pm 0.006
● YOLOv8n-Ghost-P2-PIoU (FT+AT)	1.6	7.8	8.8	0.704 \pm 0.001	0.447 \pm 0.007	0.925 \pm 0.003	0.769 \pm 0.008
F) FPGA							
★ YOLOv8s-Ghost-P2-PIoU2	5.3	5.7*	37.2 [†]	0.697	0.438	0.931	0.785
★ YOLOv8n-Ghost-P2-PIoU2	1.6	2.0*	14.6 [†]	0.704	0.445	0.921	0.765

* FPGA model size reflect quantized model sizes and are not compiled for direct comparison to baseline models.

[†] Number of operations (OPs) of the compiled FPGA model on the DPU reported instead of FLOPs as the model is quantized to INT8.

YOLOv8n-Ghost-P2-PIoU2 model is selected as the best performing architecture; it combines the smallest base model size, the efficiency improvements of the Ghost blocks, the improved detection performance with the addition of the P2 feature map and the improved accuracy of the PIoU2 loss function. We further enhanced the model through the two-stage training approach as discussed in Section II-E (Table I.E). Pre-training on pseudo-labeled data (**PT**) consistently improves fishing classification performance due to increased sample diversity, though this comes at the cost of reduced near-shore detection performance, which is likely a consequence of fewer AIS-broadcasting vessels in coastal areas, and therefore also fewer ground-truth labels. The subsequent fine-tuning stage on the validation set (**FT**) recovers these losses while maintaining classification gains,

resulting in average improvements of 1.0% in detection and 3.4% in classification compared to single-stage training. Notably, following the same training procedure, the baseline unmodified YOLOv8n model trails on average our final model by 6.5% and 1.3% in detection and classification respectively. Finally, with the adaptive thresholding method (**AT**) we are able to increase overall detection performance by 1.3% on our YOLOv8n-Ghost-P2-PIoU2 model, with a 0.4% average drop in the other metrics.

Comparing the performance of our best models to the top-5 winning entries of the xView3-SAR competition (see Fig. 3), our model nears the competition models with between 98.2% and 99.8% fewer parameters. Our detection performance is within 2.1% of the top-5 winning entries and outperforms one model in near-shore detection by 1.9%. Our

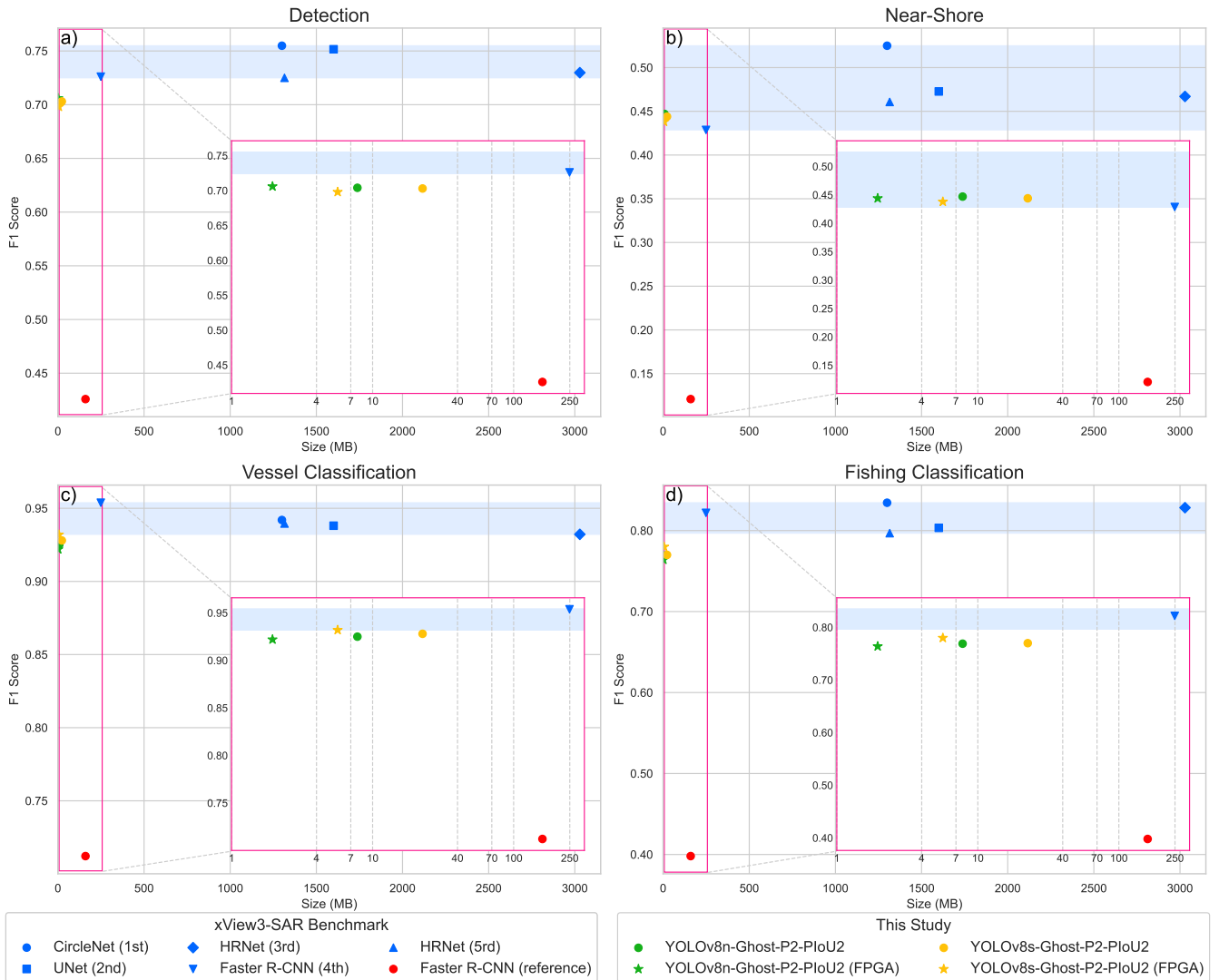


Fig. 3. F1 Score vs. Model Size (MB) for Detection (a), Near-Shore Detection (b), Vessel Classification (c), and Fishing Vessel Classification (d) tasks. In each plot, the top-5 winning models from the xView3-SAR competition are shown in blue, with the range of their F1 scores shown by the pale blue band. The competition reference model is shown by the red circle. Models from this study are shown in yellow (modified YOLOv8 small model) and green (modified YOLOv8 nano model), where floating point and quantized, FPGA-deployed models are denoted by circles and stars respectively. Inset plots in pink show a zoomed-in view of each corresponding plot between 0 and 250 MB on the x-axis (logarithmic). FPGA model results (star markers) are shown using quantized model size rather than compiled size, to enable direct comparison with the baseline models.

model is only 0.7% and 2.8% behind the top-5 in vessel and fishing classification respectively.

We also investigated several additional modifications, following methods from the literature, which did not show improvements for our implementation. Modifying the model’s FPN to AFPN or GFPN showed a performance drop across the different metrics, with slight model size increases. Similarly, incorporating attention modules (Convolutional Block Attention Module [66], CA, EMA) at the point where feature maps are fed into the FPN improved fishing classification performance by an average of 2.8%, though this came at the cost of reduced overall detection performance.

B. Quantization Results

We employ quantization to reduce model size and computational complexity, as well as to meet the constraints of

the target FPGA hardware. We evaluate quantized models on the test dataset on GPU, with results summarized in Table II. This table highlights performance differences across the baseline YOLOv8n model, as well as both the *nano* and *small* Ghost-P2 models with P1oU2 loss, all trained with our two-stage training approach.

1) *Post-Training Quantization (PTQ)*: We calibrated our models on a 1,000 image subset of the *validation* set. Smaller (100) and larger (10,000) calibration sets were also tested, but these changes did not result in significant performance differences. With PTQ, models show moderate performance degradation compared to their floating-point counterparts, with an average drop of 3.3% in detection performance and 4.2% in classification metrics. The overall detection performance decreased by 6.0% for the baseline architecture

compared to the 2.2% and 3.0% drop for our modified *small* and *nano* models respectively. These results indicate that quantization exacerbated the limitations of the less performant baseline architecture, while our modified architectures are more robust to quantization. Additionally, performance drop of the smallest model (*nano*) can be attributed to the reduced amount of redundancy with fewer parameters, which leads to a more pronounced impact.

TABLE II

PERFORMANCE OF YOLOV8 MODELS WITH INT8 PTQ AND QAT ON GPU, AND QAT ON FPGA. GPU MODEL F1-SCORES ARE PROVIDED AS MEANS AND STANDARD DEVIATIONS OVER THREE RANDOM SEEDS.

Model	F1-Score			
	Detection	Near-Shore	Vessel	Fishing
A) YOLOv8n (PT+FT+AT)				
Float	0.650±0.002	0.385±0.008	0.918±0.003	0.737±0.016
PTQ	0.627±0.005	0.347±0.008	0.851±0.042	0.626±0.067
QAT	0.646±0.004	0.377±0.011	0.915±0.002	0.725±0.018
FPGA	0.647	0.386	0.914	0.730
B) YOLOv8s-Ghost-P2-Plou2 (PT+FT+AT)				
● Float	0.703±0.004	0.444±0.010	0.928±0.003	0.770±0.013
PTQ	0.677±0.008	0.413±0.014	0.910±0.004	0.756±0.003
QAT	0.699±0.001	0.444±0.007	0.932±0.001	0.779±0.001
★ FPGA	0.697	0.438	0.931	0.785
C) YOLOv8n-Ghost-P2-Plou2 (PT+FT+AT)				
● Float	0.704±0.001	0.447±0.007	0.925±0.003	0.769±0.008
PTQ	0.667±0.011	0.408±0.012	0.903±0.014	0.747±0.022
QAT	0.701±0.003	0.445±0.001	0.927±0.005	0.771±0.009
★ FPGA	0.704	0.445	0.921	0.765

2) *Quantization-Aware Training (QAT)*: To minimize the performance drop observed with PTQ, we modify the second training stage (FT) with QAT. We use the same training parameters as the fine-tuning stage detailed in Section II-E, with the addition of a quantizer parameter learning rate 100 times larger than the model learning rate (0.5). QAT implementation introduces minimal performance degradation across most metrics (average -0.4% for detection F1), with our modified architecture models showing slight improvement in classification metrics (e.g. +0.9% for YOLOv8s-Ghost-P2-Plou2 QAT). The baseline architecture shows the highest average performance drop of 0.7%, with the *nano* modified architectures showing a loss of 0.1% and the *small* a 0.2% improvement overall. Nevertheless, the YOLOv8n-Ghost-P2-Plou2 model shows the highest detection performance overall, with a 0.701 and 0.445 F1 score for detection and near-shore detection respectively, outperforming the baseline model and the *small* model by 5.5% and 0.2% respectively. These results indicate that with QAT, most of the performance drop observed with PTQ can be recovered, and confirms that our two-stage training approach is effective for improving model performance.

C. FPGA Deployment Results

The performance of the deployed compiled QAT models on the Kria KV260 board is shown in Table II and matches the expected performance based on the GPU results, with little to no performance degradation observed. For our final

model, we also visually illustrate the quality of the results with respect to a state-of-the-art GPU-based model. From simple visual inspection of these qualitative results (Fig. 4), our FPGA-deployed model shows similar levels of performance to the xView3-SAR first-place model. We note that the winning model shows slightly higher performance overall by missing fewer detections (false negatives), at the cost of a larger number of false positives. The winning model also shows slightly higher detection performance in near-shore areas, where our model misses more detections (contrast Fig. 4.b.2 vs c.2). However, it is important to note that our model is only 0.15% of the size of the winning model (2.0 MB vs. 1294 MB, see Table I).

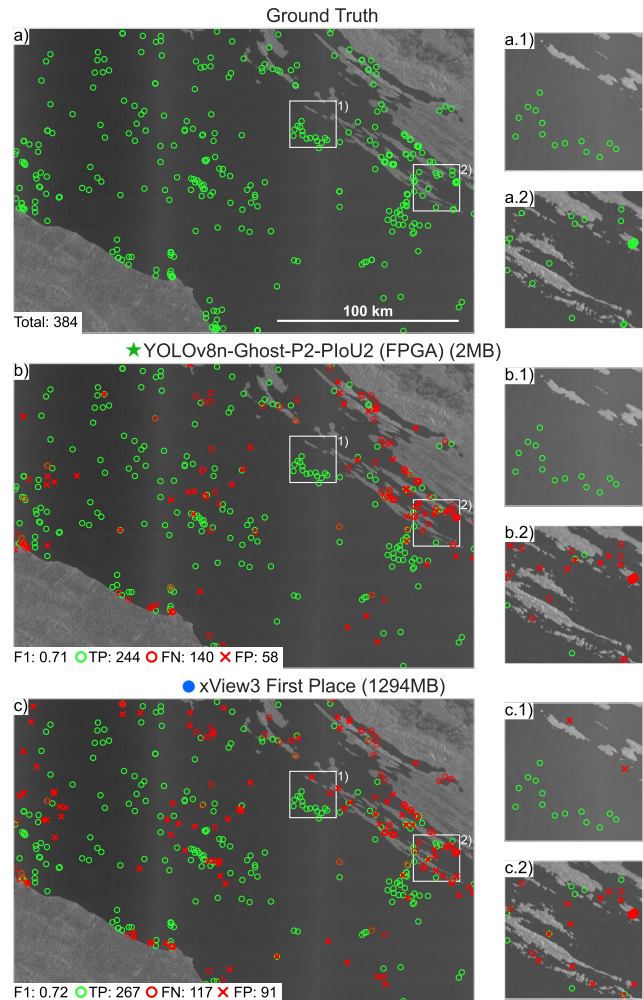


Fig. 4. Qualitative result comparison showing a sample scene from the xView3-SAR dataset with ground-truth labels (a), our proposed YOLOv8n-Ghost-P2-Plou2 model predictions on FPGA (b) and first-place competition entry (c). Zoomed-in view of areas of interest for each plot (.1, .2).

The power usage, efficiency, and throughput of the YOLOv8 model variants implemented on the Kria KV260 development board are presented in Table III. The SoC power measurements were collected using xlnx_platformstats monitoring software with a 30-second sampling window and samples taken every 0.01 seconds (100 Hz sampling rate).

TABLE III

POWER USAGE, THROUGHPUT AND EFFICIENCY OF YOLOV8 VARIANTS INFERENCE ON KRIA KV260 DEVELOPMENT BOARD ACROSS DIFFERENT THREAD CONFIGURATIONS (1, 2, 4, AND 8 THREADS)

Model	Thread (#)	Power (W)		Throughput (FPS)	Efficiency (FPS/W)
		Avg	Peak		
YOLOv8n	1	5.4	8.9	6.9	1.3
	2	6.4	9.4	12.8	2.0
	4	7.6	9.8	19.8	2.6
	8	7.8	9.8	21.6	2.8
YOLOv8n-Ghost	1	5.1	8.6	7.2	1.4
	2	6.0	9.2	13.4	2.2
	4	7.2	9.4	20.9	2.9
	8	7.3	9.7	22.9	3.1
YOLOv8n-Ghost-P2	1	4.9	9.5	3.6	0.7
	2	5.7	10.0	7.0	1.2
	4	6.9	10.5	11.8	1.7
	8	7.0	10.8	13.4	1.9
YOLOv8s-Ghost-P2	1	5.3	9.8	3.2	0.6
	2	6.5	10.2	6.2	1.0
	4	8.1	10.4	10.4	1.3
	8	8.1	10.4	10.5	1.3

Average power consumption was calculated over the full inference period, while peak power represents the highest reading recorded during operation. When idle, the SoC has a baseline consumption of 4.1 watts.

Architectural modifications to the YOLOv8n model yield distinct trade-offs on the FPGA platform. The integration of Ghost blocks enhances processing efficiency, providing an average throughput increase of 5.2% while reducing average power consumption by 5.9%. With eight threads, the YOLOv8n-Ghost model achieves 22.9 FPS, compared to 21.6 FPS for the baseline YOLOv8n. In contrast, the adoption of the P2 architecture introduces a significant performance bottleneck, decreasing throughput by an average of 47.8% (e.g. resulting in 13.4 FPS for the YOLOv8n-Ghost-P2 with eight threads) and raising peak power consumption. This degradation is attributed to the increased post-processing load from the higher-resolution feature maps, which are decoded on the CPU. The larger YOLOv8s-Ghost-P2 model suffers from further efficiency loss, with reduced throughput and no performance gains when increasing threads from 4 to 8. Nevertheless, a consistent trend was observed across all models: increasing concurrency boosts both throughput and efficiency (FPS/W); however, these gains diminish at higher thread counts and come at the cost of increased average and peak power consumption. Consequently, the number of threads can be used as a key parameter to balance performance against power constraints in a deployment scenario.

A breakdown of the inference time for different YOLOv8 model architectures is shown in Fig. 5. Image loading and pre-processing requires on average 71 ms, while DPU inference times vary by architecture. The baseline *nano* YOLOv8 model has an average inference time of 33 ms. The Ghost variant achieves a 9% reduction in latency, with an average of 30 ms, attributed to a 41% decrease in computational com-

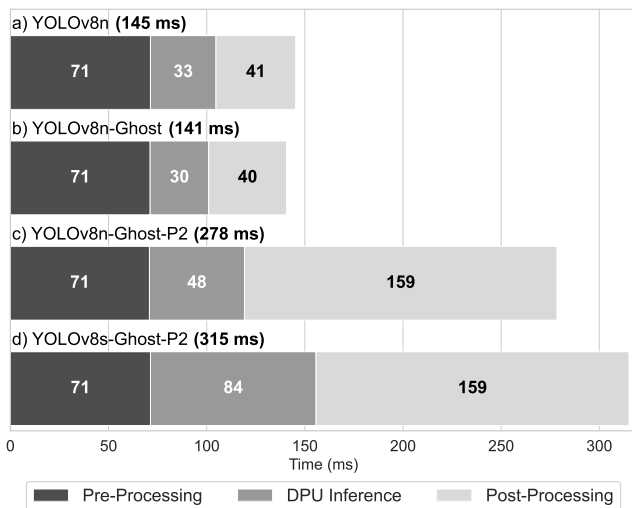


Fig. 5. Processing time breakdown of YOLOv8 variants measured on Kria KV260 development board. Each bar represents average time from 100 consecutive inference runs.

plexity. However, the speed-up is partially offset by increased memory access overhead due to higher read/write operations. The P2 variant is 60% slower (48 ms) due to its additional layers and larger feature maps. Finally, the larger *small* Ghost P2 model is the slowest at 84 ms. The post-processing step takes on average 41 ms for the baseline architectures and 159 ms for the P2 variants. The increased computation time results from the P2 feature map generating 40,000 additional predictions compared to the baseline configuration. Post-processing consists of two stages: a computationally intensive decoding step that transforms raw network outputs into bounding box coordinates, class probabilities, and confidence scores, and Non-Maximum Suppression (NMS) filtering, which requires only 91 μ s on average.

IV. DISCUSSION

In this study we have shown that highly-performant SAR vessel detection is possible in power-restricted on-satellite systems. When deployed on FPGA, our proposed YOLOv8-Ghost-P2-PIoU2 architecture has detection and classification performance only \sim 2% and \sim 3% lower than values from state-of-the-art GPU-based models on the xView3-SAR dataset, despite being \sim 130 to \sim 1500 times smaller in size. This major efficiency gain primarily stems from the synergistic effects between our choice of base model, our architectural modifications and our training modifications. YOLOv8 is an ideal base for on-satellite SAR vessel detection due to its efficient feature extraction and apparent increasing performance for this task with decreasing size of base model (Table I.A). Our architecture modifications enhance the efficiency and performance of this model even further; Ghost convolutions provide a 45% reduction in parameters and FLOPs with minimal detection performance loss, the P2 feature map contributes an additional 7.6% improvement in near-shore detection at the cost of 27.5% increased computational complexity, and the PIoU2 loss

function delivers consistent improvements across detection and classification metrics. Finally, Quantization-Aware Training was highly effective at maintaining detection accuracy on edge hardware, and our quantized model showed just 0.1% degradation in performance relative to the non-quantized model.

Together, these adaptations have produced an effective and efficient SAR vessel detection model that is highly suited for on-satellite sensing. In this section we now discuss how this model could be further adapted, used, and exploited, via: A) directions for further improvement of model performance and efficiency; B) considerations for practical on-satellite deployment of our model; C) the major changes in satellite capabilities that such on-satellite deployment could enable.

A. Potential for further improvement to model performance and efficiency

The residual performance gap between our FPGA-deployed model and larger state-of-the-art GPU-based models lies mainly in near-shore detection (0.447 vs. 0.525 F1-score compared to the top competitor from the xView3-SAR competition) and fishing classification (0.769 vs. 0.834 F1-score). This difference likely reflects a fundamental limitation of single-stage detection models in detecting small objects, where our architecture may lack the multi-scale feature fusion and high-resolution segmentation capabilities required for challenging detection scenarios that involve complex coastal environments and subtle vessel-type distinctions. In contrast, several winning xView3-SAR competitors used architectures such as UNet or HRNet, which are larger but excel at preserving the fine-grained spatial details crucial for distinguishing small vessels from complex coastal clutter. A promising alternative for achieving higher performance in lightweight models may lie in adopting architectures fundamentally different from the Convolutional Neural Network structure used here; in particular, Vision Transformers have recently shown promising results for SAR vessel detection [67]–[69], and transformer architectures have also shown potential for high performance even at extremely low bit-width, with binary and ternary compression [70], [71]. Alternatively, further performance improvements may be possible by combining our model with statistical approaches, such as combinations of CFAR and ML methods [72]. Conversely, leveraging known information on coastlines, static infrastructure or areas of interest from auxiliary datasets or from previous observations of the same area could also improve detection performance.

Given the proof-of-concept nature of this study, there are several opportunities to further improve our model’s speed of analysis, in order to support future operational deployment. In this work, we applied 8-bit quantization to the YOLOv8 models as a primary model compression technique, significantly reducing model size and efficiency while maintaining accuracy. However, additional avenues for optimisation remain. Quantization to lower bit-widths (e.g. 4-bit [73] or 1-bit [74]) or the use of mixed-precision techniques [75], [76] may offer a more favourable trade-off between

accuracy and computational efficiency. In addition, pruning redundant parameters from the model has the potential to further reduce computational load and memory usage without substantially impacting performance. Lastly, knowledge distillation presents a promising strategy to transfer knowledge from the quantized model into an even smaller and faster student model, potentially enabling real-time performance on edge devices with limited resources.

Despite the overall speed of our current analysis pipeline, it does have a significant computational bottleneck in both pre- and post-processing operations, with these steps consuming 83% of the total inference time (230 ms out of 278 ms total, see Fig. 5). Pre-processing likely carries unnecessary overhead due to our current implementation ingesting 32-bit floating point TIFF files as input, despite operating on INT8 images. And post-processing overhead arises from additional tens of thousands of outputs generated by the higher-resolution P2 feature map, which then have to undergo decoding into bounding box predictions for evaluation. Simple modifications to the decoding code achieved a 28× efficiency improvement over the baseline Vitis AI implementation, reducing processing time from 4.4s to 0.159s for the P2 architecture. This substantial gain demonstrates significant potential for additional software optimization in future. Further acceleration could be achieved by addressing pre- and post-processing bottlenecks through several strategies; for example storing image chips in lower precision formats to reduce loading times, and implementing image normalization and decoding operations directly on the FPGA using Vitis Whole Application Acceleration. These approaches would minimize memory transfer overhead and streamline the inference pipeline. Additional efficiency gains could also be realized through systematic optimization of the DPU configuration, particularly by exploring variations in parallelism levels, core counts, and operating frequencies. This potential is supported by [77], who demonstrated a 2× improvement in power efficiency on identical hardware by employing reduced parallelism (B512), four cores, and a 200 MHz frequency, suggesting similar optimizations could benefit our deployment.

B. Towards practical on-satellite deployment

The successful deployment of our model on the Kria KV260 platform demonstrates its practical viability for satellite-based maritime monitoring applications. Operating within a sub-10W power budget (average 7.0W including baseline consumption), our system meets the stringent power constraints typical of CubeSat missions while achieving the processing capability to analyze a complete SAR scene in under one minute. But in order to facilitate real-world on-satellite deployment, there are several additional important considerations.

Moving toward real-world implementation would require validating the complete processing pipeline from raw SAR data (L0) to rasterized scenes (L1) before detection, which would also require on-board SAR processing. Low-power SAR processing solutions that operate within the target

power budgets have previously been demonstrated on FPGA, [78], [79], but the total power budget would need to accommodate both SAR processing and analysis.

In addition, the choice of detection threshold and the trade-off between precision and recall is an important consideration for real-world deployment scenarios. Our model's evaluation using the xView3-SAR metrics reveals a more conservative detection approach compared to the competition's winning model, resulting in fewer false positives (FP: 10,780 vs. 12,369) but consequently higher false negatives (FN: 15,670 vs. 13,345). While this conservative threshold produces the best results in competition metrics, this threshold should be carefully chosen according to the application requirements. For example, in applications where false alarms carry significant operational costs or consequences, higher precision (lower false positive rate) may be preferable despite the increased missed detections. And conversely, in scenarios where comprehensive coverage is critical and resources are available for validation, systems optimized for high recall (lower false negative rate) would be more suitable, accepting the increased computational burden of processing additional candidate detections.

Finally, real world deployment also requires a number of other considerations; limited on-satellite storage may place constraints on the SAR processing and analysis pipeline, and fluctuating orbit-dependent power input from solar panels might introduce timing constraints on power-draw for analysis [80], [81]. Space-hardened hardware that can withstand the radiation levels encountered in low Earth orbit would also need to be investigated; a range of platforms are available for this purpose with similar capabilities to our development board, but further validation of our model would also be required on the specific hardware selected.

C. Benefits and opportunities of on-satellite SAR vessel detection

On-satellite SAR analysis would enable much faster data acquisition-to-analysis throughput than is currently possible with traditional ground-based workflows, overcoming delays caused by data downlink, processing queues, and communication latencies. Our results therefore validate the feasibility of autonomous onboard decision-making for maritime surveillance satellites, enabling immediate detection and prioritization of regions of interest without requiring ground station intervention. Integration of similar models into operational satellite constellations could enable real-time maritime domain awareness at global scales, supporting applications ranging from illegal fishing detection and maritime traffic monitoring to search and rescue operations and environmental protection enforcement.

In addition to reducing the latency of current SAR-based workflows, the feasibility of satellite-based SAR vessel detection presents significant opportunities for advancing novel autonomous satellite capabilities. There is growing interest in autonomous and distributed satellite systems [82], for example NASA's Distributed Spacecraft Autonomy project [9], and autonomous tasking and inter-satellite coordina-

tion capabilities have been identified as critical for next-generation Earth observation systems [83].

In such systems, on-satellite analysis would be used for reactive satellite-to-satellite tasking, enabling multiple satellites to work together, for example to reduce uncertainties by requesting additional data (e.g. via "tip and cue" processes [84]), potentially leveraging heterogeneous complementary sensor modalities (visual, hyperspectral, radar) and orientations. Our work validates the technical feasibility of the onboard ML processing capabilities required for such systems.

The broader implications of highly-efficient and low-power ML extend beyond maritime monitoring to other time-critical remote-sensing applications where onboard analysis can reduce latency and enable autonomous multi-platform decision-making. In the long term, development of on-board ML has the potential to transform satellite constellations from passive data collection systems into active monitoring networks that are capable of immediate response to detected events of interest; ultimately enhancing global security, environmental protection, and disaster response capabilities.

ACKNOWLEDGMENT

This work was supported by the Turing's Defence and Security programme through a partnership with Dstl. The computations described in this research were performed using the Baskerville Tier 2 HPC service. Baskerville was funded by the EPSRC and UKRI through the World Class Labs scheme (EP/T022221/1) and the Digital Research Infrastructure programme (EP/W032244/1) and is operated by Advanced Research Computing at the University of Birmingham. Copernicus Sentinel-1 SAR data are provided courtesy of the European Space Agency.

REFERENCES

- [1] R. Sunkur, K. Kantamaneni, C. Bokhoree, U. Rathnayake, and M. Fernando, "Mangrove mapping and monitoring using remote sensing techniques towards climate change resilience," *Scientific Reports*, vol. 14, no. 1, p. 6949, Mar 2024.
- [2] Y. Ban, P. Zhang, A. Nascetti, A. R. Bevington, and M. A. Wulder, "Near Real-Time Wildfire Progression Monitoring with Sentinel-1 SAR Time Series and Deep Learning," *Scientific Reports*, vol. 10, no. 1, p. 1322, Jan 2020.
- [3] R. M. Sabir, K. Mehmood, A. Sarwar, M. Safdar, N. E. Muhammad, N. Gul, F. Athar, M. D. Majeed, J. Sattar, Z. Khan, M. Fatima, M. A. Hussain, and H. M. B. Akram, *Remote Sensing and Precision Agriculture: A Sustainable Future*. Springer Nature Switzerland, 2024, pp. 75–103.
- [4] P. Boccardo and F. Giulio Tonolo, "Remote Sensing Role in Emergency Mapping for Disaster Response," in *Engineering Geology for Society and Territory - Volume 5*, G. Lollino, A. Manconi, F. Guzzetti, M. Culshaw, P. Bobrowsky, and F. Luino, Eds. Cham: Springer International Publishing, 2015, pp. 17–24.
- [5] T. J. Ma and R. J. Anderson, "Remote Sensing Low Signal-to-Noise-Ratio Target Detection Enhancement," *Sensors*, vol. 23, no. 6, 2023.
- [6] OECD, *The Space Economy in Figures: How Space Contributes to the Global Economy*. Paris: OECD Publishing, 2019.
- [7] W. Han, X. Zhang, Y. Wang, L. Wang, X. Huang, J. Li, S. Wang, W. Chen, X. Li, R. Feng, R. Fan, X. Zhang, and Y. Wang, "A survey of machine learning and deep learning in remote sensing of geological environment: Challenges, advances, and opportunities," *ISPRS Journal of Photogrammetry and Remote Sensing*, vol. 202, pp. 87–113, 2023.

- [8] H. Ouchra, A. Belangour, and A. Erraissi, "Machine learning for satellite image classification: A comprehensive review," in *2022 International Conference on Data Analytics for Business and Industry (ICDABI)*, 2022, pp. 1–5.
- [9] M. Gardill, W. Kinsner, J. Budroweit, A. Al-Hourani, E. Dunkel, J. Swope, D. Evans, and M. Staebler, "Towards Space Edge Computing and Onboard AI for Real-Time Teleoperations," in *IEEE International Conference on Cognitive Informatics and Cognitive Computing*, June 2023.
- [10] H. Heidt, J. Puig-Suari, A. S. Moore, S. Nakasuka, and R. J. Twiggs, "CubeSat: A New Generation of Picosatellite for Education and Industry Low-Cost Space Experimentation," 2000.
- [11] A. Maskey and M. Cho, "CubeSatNet: Ultralight Convolutional Neural Network designed for on-orbit binary image classification on a 1U CubeSat," *Engineering Applications of Artificial Intelligence*, vol. 96, p. 103952, 2020.
- [12] E. Rapuano, G. Meoni, T. Pacini, G. Dinelli, G. Furano, G. Giuffrida, and L. Fanucci, "An FPGA-Based Hardware Accelerator for CNNs Inference on Board Satellites: Benchmarking with Myriad 2-Based Solution for the CloudScout Case Study," *Remote Sensing*, vol. 13, no. 8, 2021.
- [13] G. Giuffrida, L. Fanucci, G. Meoni, M. Batič, L. Buckley, A. Dunne, C. van Dijk, M. Esposito, J. Hefele, N. Vercruyssen, G. Furano, M. Pastena, and J. Aschbacher, "The ϕ -Sat-1 Mission: The First On-Board Deep Neural Network Demonstrator for Satellite Earth Observation," *IEEE Transactions on Geoscience and Remote Sensing*, vol. 60, pp. 1–14, 2022.
- [14] V. Růžička, G. Mateo-García, C. Bridges, C. Brunskill, C. Purcell, N. Longépé, and A. Markham, "Fast Model Inference and Training On-Board of Satellites," in *IGARSS 2023 - 2023 IEEE International Geoscience and Remote Sensing Symposium*, 2023, pp. 2002–2005.
- [15] A. A. Kurekin, B. R. Loveday, O. Clements, G. D. Quartly, P. I. Miller, G. Wiafe, and K. Adu Agyekum, "Operational monitoring of illegal fishing in ghana through exploitation of satellite earth observation and ais data," *Remote Sensing*, vol. 11, no. 3, 2019.
- [16] A. Renga, M. Graziano, M. D'Errico, A. Moccia, and A. Cecchini, "SAR-based sea traffic monitoring: a reliable approach for Maritime Surveillance," vol. 8179, no. 2011.
- [17] H. Tanveer, N. R. Magliocca, and K. M. Curtin, "Identifying narco-trafficking landing zones using satellite imagery and geospatial indicators in Costa Rica," *GeoJournal*, vol. 90, no. 1, p. 31, Jan 2025.
- [18] T. R. Robinson, N. Rosser, and R. J. Walters, "The Spatial and Temporal Influence of Cloud Cover on Satellite-Based Emergency Mapping of Earthquake Disasters," *Scientific Reports*, vol. 9, no. 1, p. 12455, 2019.
- [19] P. K. Leong, "Securing Malaysia's maritime environment using space-derived services," *Contemporary Issues in Air and Space Power*, vol. 3, no. 1, p. bp42323989, 2025.
- [20] C. M. Awais, M. Reggiani, D. Moroni, and E. Salerno, "A Survey on SAR ship classification using Deep Learning," 2025.
- [21] Y. Li, W. Zhu, and B. Zhu, "SAR Image Nearshore Ship Target Detection in Complex Environment," in *2021 IEEE 5th Advanced Information Technology, Electronic and Automation Control Conference (IAEAC)*, 2021, pp. 1964–1968.
- [22] European Space Agency, *Sentinel-1: ESA's Radar Observatory Mission for GMES Operational Services*, ser. Special Publications, K. Fletcher, Ed. Noordwijk, The Netherlands: ESA Communications, 2012, vol. 1322, eSA SP, ISSN 0379-6566. Volume 1 of SENTINEL / production ed.: Karen Fletcher.
- [23] JAXA, "Advanced Land Observing Satellite-4 "Daichi-4" [Technical overview]," n.d., retrieved from <https://global.jaxa.jp/projects/sat/alos4/>.
- [24] NASA-ISRO SAR (NISAR), "Mission Science Users' Handbook," NASA Jet Propulsion Laboratory, Tech. Rep., 2018, 1: NISAR.
- [25] J. R. Elliott, R. J. Walters, and T. J. Wright, "The role of space-based observation in understanding and responding to active tectonics and earthquakes," *Nature Communications*, vol. 7, no. 1, p. 13844, 2016.
- [26] X. X. Zhu, S. Montazeri, M. Ali, Y. Hua, Y. Wang, L. Mou, Y. Shi, F. Xu, and R. Bamler, "Deep Learning Meets SAR: Concepts, models, pitfalls, and perspectives," *IEEE Geoscience and Remote Sensing Magazine*, vol. 9, no. 4, pp. 143–172, 2021.
- [27] M. Yasir, A. J. Niang, M. S. Hossain, Q. U. Islam, Q. Yang, and Y. Yin, "Ranking Ship Detection Methods Using SAR Images Based on Machine Learning and Artificial Intelligence," *Journal of Marine Science and Engineering*, vol. 11, no. 10, 2023.
- [28] K. El-Darymli, C. Gierull, and K. Biron, "Deep learning vs. K-CFAR for ship detection in spaceborne SAR imagery," 07 2024, pp. 8037–8040.
- [29] F. Paolo, T. ting Tim Lin, R. Gupta, B. Goodman, N. Patel, D. Kuster, D. Kroodsmas, and J. Dunnmon, "xView3-SAR: Detecting Dark Fishing Activity Using Synthetic Aperture Radar Imagery," 2022.
- [30] F. Meng, X. Qi, and H. Fan, "LSR-Det: A Lightweight Detector for Ship Detection in SAR Images Based on Oriented Bounding Box," *Remote Sensing*, vol. 16, no. 17, 2024.
- [31] M. Cao, W. Xie, J. Lei, J. Zhang, D. Li, and Y. Li, "Multi-scale direction-aware SAR object detection network via global information fusion," 2024.
- [32] S. Zhao, R. Tao, and F. Jia, "DML-YOLOv8-SAR image object detection algorithm," *Signal, Image and Video Processing*, vol. 18, no. 10, pp. 6911–6923, 2024.
- [33] M. Yasir, S. Liu, S. Pirasteh, M. Xu, H. Sheng, J. Wan, F. A. de Figueiredo, F. J. Aguilár, and J. Li, "YOLOShipTracker: Tracking ships in SAR images using lightweight YOLOv8," *International Journal of Applied Earth Observation and Geoinformation*, vol. 134, p. 104137, 2024.
- [34] S. Zhu and M. Miao, "Lightweight high-precision SAR ship detection method based on YOLOv7-LDS," *PLOS ONE*, vol. 19, no. 2, pp. 1–26, 02 2024.
- [35] Y. Gao, W. Hua, H. Tian, Z. Sun, M. Cai, and Y. Guo, "Object Detection for SAR Ship Images Based on YOLOv5 Deployed On Jetson AGX Xavier," in *2022 3rd China International SAR Symposium (CISS)*, 2022, pp. 1–4.
- [36] G. Yang, J. Lei, W. Xie, Z. Fang, Y. Li, J. Wang, and X. Zhang, "Algorithm/Hardware Codesign for Real-Time On-Satellite CNN-Based Ship Detection in SAR Imagery," *IEEE Transactions on Geoscience and Remote Sensing*, vol. 60, pp. 1–18, 2022.
- [37] X. Huang, K. Xu, J. Chen, A. Wang, S. Chen, and H. Li, "Real-Time Processing of Ship Detection with SAR Image Based on FPGA," in *IGARSS 2024 - 2024 IEEE International Geoscience and Remote Sensing Symposium*, 2024, pp. 8954–8957.
- [38] N. Fang, L. Li, X. Zhou, W. Zhang, and F. Chen, "An FPGA-Based Hybrid Overlapping Acceleration Architecture for Small-Target Remote Sensing Detection," *Remote Sensing*, vol. 17, no. 3, 2025.
- [39] T. Zhang, X. Zhang, J. Li, X. Xu, B. Wang, X. Zhan, Y. Xu, X. Ke, T. Zeng, H. Su, I. Ahmad, D. Pan, C. Liu, Y. Zhou, J. Shi, and S. Wei, "SAR Ship Detection Dataset (SSDD): Official Release and Comprehensive Data Analysis," *Remote Sensing*, vol. 13, no. 18, 2021.
- [40] Y. Wang, C. Wang, H. Zhang, Y. Dong, and S. Wei, "A SAR Dataset of Ship Detection for Deep Learning under Complex Backgrounds," *Remote Sensing*, vol. 11, no. 7, 2019.
- [41] S. Wei, X. Zeng, Q. Qu, M. Wang, H. Su, and J. Shi, "HRSID: A High-Resolution SAR Images Dataset for Ship Detection and Instance Segmentation," *IEEE Access*, vol. 8, pp. 120234–120254, 2020.
- [42] RangeKing, "Ultralytics YOLOv8 Architecture Diagram," <https://github.com/ultralytics/ultralytics/issues/189>, 2023, Accessed: 2025-06-13.
- [43] J. Redmon, S. Divvala, R. Girshick, and A. Farhadi, "You Only Look Once: Unified, Real-Time Object Detection," in *2016 IEEE Conference on Computer Vision and Pattern Recognition (CVPR)*. Los Alamitos, CA, USA: IEEE Computer Society, Jun. 2016, pp. 779–788.
- [44] Y. Luo, M. Li, G. Wen, Y. Tan, and C. Shi, "SHIP-YOLO: A Lightweight Synthetic Aperture Radar Ship Detection Model Based on YOLOv8n Algorithm," *IEEE Access*, vol. 12, pp. 37030–37041, 2024.
- [45] J. He and C. Huang, "YOLOv8-SARship: An Efficient and Accurate Detection Method for SAR Ship Images," in *5th International Conference on Computer Vision, Image and Deep Learning (CVIDL)*, 2024, pp. 280–284.
- [46] B. Khalili and A. W. Smyth, "SOD-YOLOv8—Enhancing YOLOv8 for Small Object Detection in Aerial Imagery and Traffic Scenes," *Sensors*, vol. 24, no. 19, 2024.
- [47] A. Bochkovskiy, C.-Y. Wang, and H.-Y. M. Liao, "YOLOv4: Optimal Speed and Accuracy of Object Detection," 2020.
- [48] T.-Y. Lin, P. Dollár, R. Girshick, K. He, B. Hariharan, and S. Belongie, "Feature Pyramid Networks for Object Detection," in *2017 IEEE Conference on Computer Vision and Pattern Recognition (CVPR)*, 2017, pp. 936–944.
- [49] S. Liu, L. Qi, H. Qin, J. Shi, and J. Jia, "Path Aggregation Network for Instance Segmentation," in *2018 IEEE/CVF Conference on Computer Vision and Pattern Recognition*, 2018, pp. 8759–8768.

- [50] T. D. Bui and T. M. Do Le, "Ghost-Attention-YOLOv8: Enhancing Rice Leaf Disease Detection with Lightweight Feature Extraction and Advanced Attention Mechanisms," *AgriEngineering*, vol. 7, no. 4, 2025.
- [51] X. Xiao and X. Feng, "Multi-Object Pedestrian Tracking Using Improved YOLOv8 and OC-SORT," *Sensors*, vol. 23, p. 8439, 10 2023.
- [52] X. Guo and B. Xu, "SAR-NTV-YOLOv8: A Neural Network Aircraft Detection Method in SAR Images Based on Despeckling Preprocessing," *Remote Sensing*, vol. 16, no. 18, 2024.
- [53] M. Kang, C.-M. Ting, F. F. Ting, and R. C.-W. Phan, "BGF-YOLO: Enhanced YOLOv8 with Multiscale Attentional Feature Fusion for Brain Tumor Detection," in *Proceedings of Medical Image Computing and Computer Assisted Intervention – MICCAI 2024*, vol. LNCS 15008. Springer Nature Switzerland, October 2024.
- [54] D. Ouyang, S. He, G. Zhang, M. Luo, H. Guo, J. Zhan, and Z. Huang, "Efficient Multi-Scale Attention Module with Cross-Spatial Learning," in *ICASSP 2023 - 2023 IEEE International Conference on Acoustics, Speech and Signal Processing (ICASSP)*. IEEE, Jun. 2023, p. 1–5.
- [55] F. Feng, Y. Hu, W. Li, and F. Yang, "Improved YOLOv8 algorithms for small object detection in aerial imagery," *Journal of King Saud University - Computer and Information Sciences*, vol. 36, no. 6, p. 102113, 2024.
- [56] Q. Hou, D. Zhou, and J. Feng, "Coordinate attention for efficient mobile network design," in *2021 IEEE/CVF Conference on Computer Vision and Pattern Recognition (CVPR)*, 2021, pp. 13 708–13 717.
- [57] K. Han, Y. Wang, Q. Tian, J. Guo, C. Xu, and C. Xu, "GhostNet: More Features from Cheap Operations," 2020.
- [58] C. Liu, K. Wang, Q. Li, F. Zhao, K. Zhao, and H. Ma, "Powerful-IoU: More straightforward and faster bounding box regression loss with a nonmonotonic focusing mechanism," *Neural Networks*, vol. 170, pp. 276–284, 2024.
- [59] S. Jain, A. Gural, M. Wu, and C. Dick, "Trained Quantization Thresholds for Accurate and Efficient Fixed-Point Inference of Deep Neural Networks," in *Proceedings of Machine Learning and Systems*, I. Dhillon, D. Papailiopoulos, and V. Sze, Eds., vol. 2, 2020, pp. 112–128.
- [60] A. Howard, M. Sandler, G. Chu, L.-C. Chen, B. Chen, M. Tan, W. Wang, Y. Zhu, R. Pang, V. Vasudevan, Q. V. Le, and H. Adam, "Searching for mobilenetv3," 2019.
- [61] G. B. C. G. 2019, "The GEBCO2019 Grid - a continuous terrain model of the global oceans and land," *Published Data Library (PDL)*, 2019.
- [62] H. Lang, R. Wang, S. Zheng, S. Wu, and J. Li, "Ship Classification in SAR Imagery by Shallow CNN Pre-Trained on Task-Specific Dataset with Feature Refinement," *Remote Sensing*, vol. 14, no. 23, 2022.
- [63] M. Tan and Q. Le, "EfficientNet: Rethinking Model Scaling for Convolutional Neural Networks," in *Proceedings of the 36th International Conference on Machine Learning*, ser. Proceedings of Machine Learning Research, K. Chaudhuri and R. Salakhutdinov, Eds., vol. 97. PMLR, 09–15 Jun 2019, pp. 6105–6114.
- [64] N. Ma, X. Zhang, H.-T. Zheng, and J. Sun, "ShuffleNet V2: Practical Guidelines for Efficient CNN Architecture Design," in *Proceedings of the European Conference on Computer Vision (ECCV)*, September 2018.
- [65] J. Chen, S.-h. Kao, H. He, W. Zhuo, S. Wen, C.-H. Lee, and S.-H. G. Chan, "Run, Don't Walk: Chasing Higher FLOPS for Faster Neural Networks," in *Proceedings of the IEEE/CVF Conference on Computer Vision and Pattern Recognition (CVPR)*, June 2023, pp. 12 021–12 031.
- [66] S. Woo, J. Park, J.-Y. Lee, and I. S. Kweon, "CBAM: Convolutional Block Attention Module," in *Proceedings of the European Conference on Computer Vision (ECCV)*, September 2018.
- [67] M. Ahmed, N. El-Sheimy, and H. Leung, "A Novel Detection Transformer Framework for Ship Detection in Synthetic Aperture Radar Imagery Using Advanced Feature Fusion and Polarimetric Techniques," *Remote Sensing*, vol. 16, no. 20, 2024.
- [68] R. Gupta, S. Li, T. Zhu, J. Malik, T. Darrell, and K. Mangalam, "xT: nested tokenization for larger context in large images," in *Proceedings of the 41st International Conference on Machine Learning*, ser. ICML'24. JMLR.org, 2024.
- [69] Y. Zhang, J. Cao, Y. You, and Y. Qiao, "DenSe-AdViT: A novel Vision Transformer for Dense SAR Object Detection," 2025. [Online]. Available: <https://arxiv.org/abs/2504.13638>
- [70] S. Xu, Y. Li, T. Ma, B.-W. Zeng, B. Zhang, P. Gao, and J. Lv, "TerViT: An Efficient Ternary Vision Transformer," *ArXiv*, vol. abs/2201.08050, 2022.
- [71] Y. He, Z. Lou, L. Zhang, J. Liu, W. Wu, H. Zhou, and B. Zhuang, "BiViT: Extremely Compressed Binary Vision Transformers," in *2023 IEEE/CVF International Conference on Computer Vision (ICCV)*, 2023, pp. 5628–5640.
- [72] X. Wen, S. Zhang, J. Wang, T. Yao, and Y. Tang, "A CFAR-Enhanced Ship Detector for SAR Images Based on YOLOv5s," *Remote Sensing*, vol. 16, no. 5, 2024.
- [73] Z. Yan, B. Zhang, and D. Wang, "An FPGA-Based YOLOv5 Accelerator for Real-Time Industrial Vision Applications," *Micromachines*, vol. 15, no. 9, 2024.
- [74] D. Zhang, Z. Liang, R. Cen, Z. Yan, R. Wan, and D. Wang, "HE-BiDet: A Hardware Efficient Binary Neural Network Accelerator for Object Detection in SAR Images," *Micromachines*, vol. 16, no. 5, 2025.
- [75] D. T. Nguyen, H. Kim, and H.-J. Lee, "Layer-specific optimization for mixed data flow with mixed precision in fpga design for cnn-based object detectors," *IEEE Transactions on Circuits and Systems for Video Technology*, vol. 31, no. 6, pp. 2450–2464, 2021.
- [76] A. Montgomerie-Corcoran, P. Toupas, Z. Yu, and C.-S. Bouganis, "SATAY: A Streaming Architecture Toolflow for Accelerating YOLO Models on FPGA Devices," in *2023 International Conference on Field Programmable Technology (ICFPT)*, 2023, pp. 179–187.
- [77] F. Hamanaka, T. Odan, K. Kise, and T. V. Chu, "An Exploration of State-of-the-Art Automation Frameworks for FPGA-Based DNN Acceleration," *IEEE Access*, vol. 11, pp. 5701–5713, 2023.
- [78] M. Kerr, S. Tonetti, S. Cornara, J.-I. Bravo, R. Hinz, A. Latorre, F. Membibre, C. Solimini, S. Wiehle, H. Breit, B. Tings, O. Koudelka, F. Teschl, E. Magli, T. Bianchi, A. Migliorati, P. Motto Ros, M. Caon, R. Freddi, M. Benetti, F. Milani, G. Curci, S. Fraille, L. Garcia, C. Marcos, and A. Fiengo, "EO-ALERT: A Novel Architecture for the Next Generation of Earth Observation Satellites Supporting Rapid Civil Alert," in *71st International Astronautical Congress (IAC 2020)*, October 2020.
- [79] E. I. Baungarten-Leon, G. D. Martín-del Campo-Becerra, S. Ortega-Cisneros, M. Schlemmon, J. Rivera, and A. Reigber, "Towards On-Board SAR Processing with FPGA Accelerators and a PCIe Interface," *Electronics*, vol. 12, no. 12, 2023.
- [80] J. Lee, E. Kim, and K. G. Shin, "Design and Management of Satellite Power Systems," in *2013 IEEE 34th Real-Time Systems Symposium*, 2013, pp. 97–106.
- [81] S. Lim and C. Xiaofang, "High performance on-board processing and storage for satellite remote sensing applications," in *2014 IEEE International Conference on Aerospace Electronics and Remote Sensing Technology*, 2014, pp. 137–141.
- [82] C. Araguz, E. Bou-Balust, and E. Alarcón, "Applying autonomy to distributed satellite systems: Trends, challenges, and future prospects," *Systems Engineering*, vol. 21, no. 5, pp. 401–416, 2018.
- [83] K. Thangavel, R. Sabatini, A. Gardi, K. Ranasinghe, S. Hilton, P. Servidia, and D. Spiller, "Artificial Intelligence for Trusted Autonomous Satellite Operations," *Progress in Aerospace Sciences*, vol. 144, p. 100960, 2024.
- [84] B. Cudzilo, K. Foley, and C. Smith, "The Ability of a Small Satellite Constellation to Tip and Cue Other Commercial Assets," in *26th Annual AIAA/USU Conference on Small Satellites*, no. SSC12-IV-5, 2012.